Protecting the Quantum Interference of Cat States by Phase-Space Compression

Xiaozhou Pan,[1,*,†] Jonathan Schwinger,[1,*,‡] Ni-Ni Huang,[1] Pengtao Song,[1] Weipin Chua,[2] Fumiya Hanamura,[3] Atharv Joshi,[1] Fernando Valadares,[1] Radim Filip,[4] and Yvonne Y. Gao[1,2,§]

[1]*Centre for Quantum Technologies, National University of Singapore, Singapore 117543, Singapore*
[2]*Department of Physics, National University of Singapore, Singapore 119077, Singapore*
[3]*Department of Applied Physics, School of Engineering, The University of Tokyo, Tokyo 113-8656, Japan*
[4]*Department of Optics, Palacky University, Olomouc 77146, Czech Republic*

(Received 6 December 2022; revised 7 February 2023; accepted 28 February 2023; published 7 April 2023)

Cat states, with their unique phase-space interference properties, are ideal candidates for understanding fundamental principles of quantum mechanics and performing key quantum information processing tasks. However, they are highly susceptible to photon loss, which inevitably diminishes their quantum non-Gaussian features. Here, we protect these non-Gaussian features against photon loss by compressing the phase-space distribution of a cat state. We achieve this compression with a deterministic technique based on the echoed conditional displacement operation in a circuit QED device. We present a versatile technique for creating robust non-Gaussian continuous-variable resource states in a highly linear bosonic mode and manipulating their phase-space distribution to achieve enhanced resilience against photon loss. Such compressed cat states offer an attractive avenue for obtaining new insights into quantum foundations and quantum metrology, as well as for developing inherently more protected bosonic code words for quantum error correction.

DOI: 10.1103/PhysRevX.13.021004 Subject Areas: Quantum Physics, Quantum Information

Schrödinger's cat state is a superposition of macroscopically distinct quantum states, famous from the iconic gedanken experiment of a cat being simultaneously dead and alive [1]. This concept morphed into the simplified version of a superposition of two sufficiently large (i.e., negligibly overlapping) coherent states with opposite phases, i.e., $|\alpha\rangle \pm |-\alpha\rangle$. Such large cat states are of great interest because they exhibit unique nonclassical attributes such as sub-Planck phase-space structures [2] and non-Gaussian interference features [3–5]. Apart from being a gateway to better understand the fundamental physics of quantum decoherence [6], cat states also act as the backbone for continuous-variable (CV) quantum information processing, ranging from quantum metrology [7–11], quantum teleportation, and cryptography [12–16] to the development of error-correcting codes for fault-tolerant quantum computing [17,18] by tracking the photon parity as the error syndrome in a hardware-efficient manner [19–30].

The appeals of the cat state's distinctive quantum non-Gaussian interference characteristics for probing fundamental physics and CV quantum information applications have motivated significant experimental efforts to create and manipulate them in various hardware platforms, such as optical systems [31–35], vibrational states of a trapped ion [36,37], Rydberg atoms [38,39], and circuit quantum electrodynamics (cQED) [40,41]. In particular, the cQED platform in the form of 3D superconducting cavities controlled by one or more nonlinear ancillary modes has enabled the creation [40] as well as universal control [42,43] of large and highly coherent cat states, making it an excellent candidate for storing and manipulating quantum information and non-Gaussian resource states [44–46]. However, the desired interference features of cat states, formed by the coherent superposition of $\pm|\alpha\rangle$, are notoriously delicate. Their rapid decay under photon loss, the dominant error channel of the cavity mode, directly signifies the loss of quantum non-Gaussian characteristics [47–55].

Preservation of these quantum interference features in cat states can be deterministically achieved by phase-space compression. The characteristic function describes the spectral landscape of quantum states, where the features further away from the origin are higher in frequency. As shown in Fig. 1(a), the interference blobs of cat states reside

*These authors contributed equally to this work.
†Corresponding author.
xiaozhou@nus.edu.sg
‡Corresponding author.
jschwinger@u.nus.edu
§Corresponding author.
yvonne.gao@nus.edu.sg

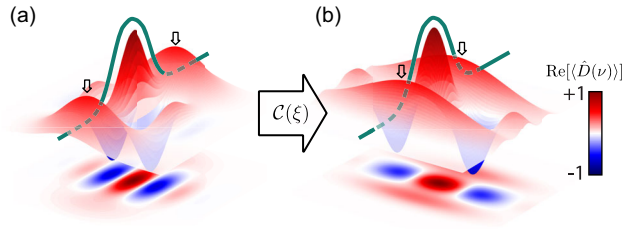

FIG. 1. Protection of quantum interference against photon loss. (a) Cat states created in superconducting cavities suffer predominantly from photon loss, which acts as a symmetric low-pass Gaussian filter (green) with width determined by $\sim 1/\kappa t$ in the characteristic function representation, where κ is the rate of photon loss. The quantum interference features, represented by the amplitude of the blobs (black arrows), diminish substantially over time as they are composed of higher-frequency components, which are more susceptible to the low-pass filter imposed by photon loss. (b) Preservation of the quantum non-Gaussianity can be achieved by compressing the phase space of the cat states, symbolized by the arrow with the compression coefficient ξ. Under the action of the compression operation, the interference blobs are pushed closer to the origin. This makes the resulting state significantly less susceptible to the filter and effectively preserves its quantum interference features against photon loss.

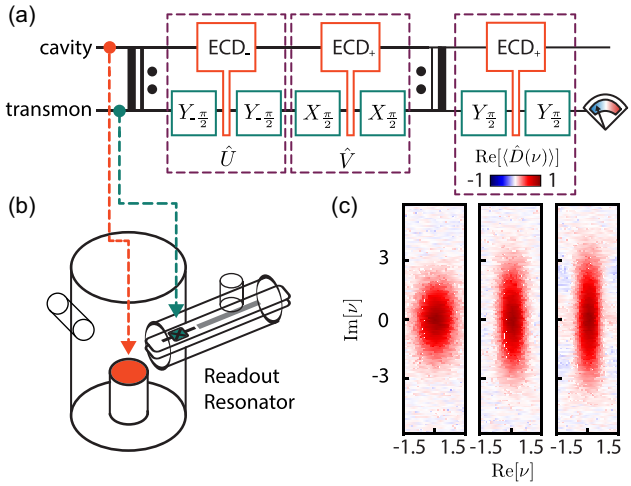

FIG. 2. Deterministic phase-space compression in cQED. (a) With vacuum as the initial state, the protocol generates compressed vacuum states based on Ref. [72]. An additional $\hat{V}$ operation followed by a single-shot readout is used to create the compressed cat states; see Appendix B. The $\hat{U}$ and $\hat{V}$ operations are each decomposed into two transmon rotations and one ECD gate. The resulting states are measured by their characteristic functions, which are obtained using the ECD gate; see Appendix C. (b) Color-coded schematic of the device showing the storage cavity, transmon, and readout mode. (c) Real part of the characteristic functions of compressed vacuum states generated by three repetitions of the $\hat{U}\hat{V}$ operations with phase-space compression of -3, -6.7, and -7.6 dB along $\mathrm{Re}[\nu]$, respectively.

at $\pm 2|\alpha|$ from origin and, therefore, correspond to high-frequency components in the characteristic function. Thus, their amplitudes diminish significantly under the effect of photon loss, which can be modeled as a pointwise scaling and multiplication with a low-pass Gaussian filter [56]. Phase-space compression, shown in Fig. 1(b), deterministically reshapes the characteristic function such that these higher-frequency elements can fit within the low-pass filter. Thus, the interference features of a compressed cat state are intrinsically more protected from the action of the Gaussian filtering due to photon loss [57–63]. While the creation of compressed cat states has been shown in quantum optics [33,64] and ion trap devices [65,66], their time dynamics and resilience against photon loss have only been experimentally probed using an optical parametric process [61]. This is because implementing fast nonlinear controls to create cat states and perform phase-space compression on them without introducing excessive nonlinearity in the quantum harmonic oscillator is challenging.

In this work, we demonstrate the deterministic protection of the quantum non-Gaussian interference features of cat states by engineering their phase-space distribution to be more compact. To realize this compression of cat states, we use the versatile conditional displacement operation, which employs only native single cavity and transmon gates, to generate a superposition of compressed coherent states. We directly probe the time dynamics of quantum coherence using features in the characteristic function and demonstrate enhanced resilience of the compressed cat's quantum non-Gaussian interference features in the presence of intrinsic losses within the hardware. Our technique offers a highly versatile operation for the creation and storage of CV resource states in bosonic modes with minimal anharmonicity. More generally, our study illustrates a powerful framework for enhancing the noise resilience of bosonic quantum states by using universal features of the echoed conditional displacement gates [67] to engineer and reshape their phase space to be more optimal against the local loss mechanisms [62]. Furthermore, our realization of the compressed cat states provides an important new ingredient to implement more intrinsically protected logical code words for fault-tolerant quantum computing [20,68–71] and is a promising candidate for quantum metrology [7–11].

Our experimental setup is a three-dimensional (3D) cQED architecture, where a 3D cavity couples to a planar chip containing an ancillary transmon and a low-Q readout resonator, as shown in Fig. 2(b). The 3D cavity, machined out of high-purity (4N) aluminium, provides a high-Q bosonic mode for the creation and storage of CV quantum states. The tasks of performing phase-space compression and storing large compressed cat states over time requires the cavity to inherit minimal anharmonicity from the transmon. As such states occupy a large span of energy levels in the harmonic oscillator, they suffer from significant distortions in phase space even in the presence of moderate nonlinearity in the cavity. Therefore, we design the system to have a weak dispersive coupling, with

$\chi/2\pi \approx 40$ kHz. This effectively suppresses the inherited nonlinearity of the bosonic mode to $K/2\pi \approx 10$ Hz. Considering the negligible cavity nonlinearity, our system is well described by the dispersive Hamiltonian $\hat{\mathbf{H}}(\mathbf{t})/\hbar = -(\chi/2)\hat{\mathbf{a}}^\dagger\hat{\mathbf{a}}\sigma_\mathbf{z}$, where $\hat{\mathbf{a}}$ and $\hat{\mathbf{a}}^\dagger$ are the annihilation and creation operators of the cavity mode and $\sigma_\mathbf{z}$ the Pauli Z operator of the transmon.

While these device parameters ensure that our cavity is a good harmonic oscillator, they come at the cost of reduced controllability as we typically rely on a larger χ to perform universal gates on the bosonic mode [43,73]. Here, we sidestep this limitation by employing a technique called echoed conditional displacement (ECD) [67,74]. The ECD gate takes advantage of large cavity displacements α_0, which act as an extended lever in phase space such that a phase that is dependent on the transmon state can be rapidly accumulated despite a small χ. This method allows conditional displacement operations to be enacted in a duration $\propto (1/\chi\alpha_0)$ instead of $\propto (1/\chi)$, and thus makes it possible to balance the need for minimizing nonlinearity and effecting universal control on the cavity [67].

Practically, the ECD gate can be readily realized on standard cQED devices. The operation requires only single transmon rotations and unconditional cavity displacements. The echo arises from a π pulse played in the middle of the sequence to suppress low-frequency noise on the transmon. Following the technique introduced in Refs. [67,74], we can enact the following effective Hamiltonian:

$$\frac{\hat{\mathbf{H}}(t)}{\hbar} = -\frac{\chi}{2}[\alpha(t)\hat{\mathbf{a}}^\dagger + \alpha^*(t)\hat{\mathbf{a}}]\sigma_\mathbf{z}, \tag{1}$$

where $\alpha(t)$ is the cavity's classical response in the presence of the resonant displacement pulses. Under Eq. (1), an ECD unitary operation, given by

$$\mathrm{ECD}_\pm(\alpha) = \hat{D}\left(+\frac{\alpha}{2}\right)|g\rangle\langle e| \pm \hat{D}\left(-\frac{\alpha}{2}\right)|e\rangle\langle g|, \tag{2}$$

is enacted on the cavity-transmon system, such that the phase of the cavity displacement is dependent on the transmon state. The phase of the superposition depends on the phase of the qubit echo pulse, plus corresponds to a X_π rotation and minus to a Y_π rotation. In our device, we can perform an ECD gate with $\alpha = 1$ in 688 ns, which compares favorably with the cavity's single-photon lifetime of $T_1^c = 260$ μs and dephasing timescale of $T_\phi^c \approx 5$ ms, and with the transmon's coherence properties of $T_1^q = 18$ μs and $T_{2e}^q = 20$ μs; see Appendix A.

Building upon the ECD gate, we implement a deterministic compression protocol to generate compressed vacuum states with the technique proposed in Ref. [72]. This procedure relies on two unitary operations $\hat{U}_k$ and $\hat{V}_k$, where $\hat{U}_k = \exp(iu_k\hat{P}\hat{\sigma}_x)$ and $\hat{V}_k = \exp(iv_k\hat{X}\hat{\sigma}_y)$, with $\hat{X} = (\hat{a} + \hat{a}^\dagger)/2$ and $\hat{P} = i(\hat{a}^\dagger - \hat{a})/2$. Conceptually, $\hat{U}_k$ displaces the cavity by an amount proportional to u_k in opposite directions in phase space depending on the transmon state, while $\hat{V}_k$ approximately disentangles cavity and transmon. Then, one set of $\hat{U}\hat{V}$ brings the initial vacuum state into two coherent states with opposite phases. Because of the interference of these two components, the resulting cavity state is compressed in one quadrature and elongated in the other. The $\hat{U}$ and $\hat{V}$ operations can be readily implemented experimentally in our system through the following decomposition,

$$\hat{U}_k = R_y\left(-\frac{\pi}{2}\right)\mathrm{ECD}_-(u_k)R_y\left(-\frac{\pi}{2}\right), \tag{3}$$

$$\hat{V}_k = R_x\left(\frac{\pi}{2}\right)\mathrm{ECD}_+(iv_k)R_x\left(\frac{\pi}{2}\right), \tag{4}$$

which features ECD gates and numerically optimized coefficients u_k and v_k. Repeating them with the appropriate coefficients allows us to create a superposition of 2^N coherent states with a Gaussian distribution, which is effectively an approximate squeezed vacuum state [Fig. 2(a)]. This procedure mimics the action of squeezing in a previous study that used an optical parametric process [61]. However, our gate-based technique offers enhanced versatility and can be extended to achieve other forms of phase-space engineering afforded by the universality of the ECD operations [67].

Based on the above strategy, we generate three vacuum states with −3, −6.7, and −7.6 dB of compression in one quadrature. To achieve this, we use three steps of the $\hat{U}\,\hat{V}$ operations and optimize the interaction parameters, u_k and v_k, for maximum overlap with the target squeezed states. We then employ the ECD gate to perform characteristic function tomography; see Appendix C. The real parts of the measured characteristic functions are shown in Fig. 2(c). Theoretically, each additional step of $\hat{U}\,\hat{V}$ increases the possible degree of compression by 3–4 dB. However, practically, the transmon's $T_{2e}^q \sim 20$ μs imposes a limit of three repetitions, which nonetheless allows us to achieve up to −7.6 dB reduction in the width of the Gaussian distribution in the $\mathrm{Re}[\nu]$ quadrature in ∼4 μs. While the deviation from ideal squeezing is apparent, it does not undermine the protocol's effectiveness in compressing the characteristic function of the vacuum state.

Using these compressed vacuum states as the input, we create compressed cat states using an additional $\hat{V}$ operation, followed by a single-shot measurement of the transmon via a DJJAA quantum amplifier [75]. The $\hat{V}$ gate conditionally displaces the compressed cavity state in opposite directions in phase space. As a result, the transmon's ground state is entangled with a compressed even cat state, and its excited state is entangled with the odd one. We then utilize the single-shot measurement to project the transmon state before performing the characteristic

function measurement. In our scheme, the compressed cat is realized by creating a superposition of compressed coherent states instead of applying the compression on a conventional cat state. While our technique is capable of both approaches, we choose the former in this work, as it is more technically favorable for the coherence parameters of our system; see Appendix D. In practice, these options for implementing compressed cat states are equivalent up to a different displacement amplitude, which arises from transforming the displacement operator with the squeezing operator, $\hat{D}(\alpha)\hat{S}(z) = \hat{S}(z)\hat{S}^{\dagger}(z)\hat{D}(\alpha)\hat{S}(z) = \hat{S}(z)\hat{D}(\gamma)$, with $\gamma = \alpha\cosh r + \alpha^{*}e^{i\theta}\sinh r$, where r is the degree of squeezing and θ the phase. We account for this displacement adjustment in our protocol to ensure that the resulting states are equivalent to a squeezed cat state with amplitude γ.

With this technique, we are able to create compressed cat states of size $|\alpha| = 1.8$, $\xi \approx -6.7$ dB and the desired photon number parity. The real parts of the measured characteristic function for cat (top) and compressed cat states (bottom) of different parities are shown in Fig. 3. The effect of the phase-space compression is indicated by the concentration of the interference blobs closer to the origin and their elongation in the opposite direction. This elongation does not influence quantum non-Gaussian features of sub-Planck oscillations but, notably, could impair the parity preservation at high compression levels; see Appendix E. For these states, the center fringes of the characteristic function indicate the mixture of the coherent amplitudes $\pm\alpha$, with the origin point always being positive. More rapid oscillations in these fringes correspond to larger amplitudes of the cat state. The presence of two blobs along $\mathrm{Re}[\nu]$ directly represents quantum non-Gaussian interference.

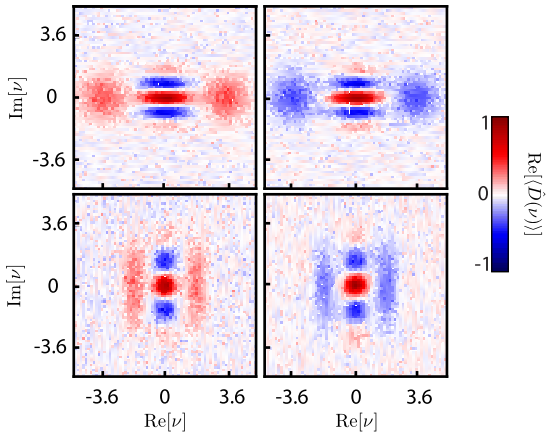

FIG. 3. Characteristic functions of cat and compressed cat states. Real part of the measured characteristic function of even and odd cat states of size $|\alpha| = 1.8$ with 0 dB (top) and approximately −6.7 dB (bottom) compression. The blobs, which correspond to quantum interference, are centered at $2|\alpha| \approx 3.6$ and $2|\alpha| \approx 1.8$, respectively. They also reflect the photon number parity of the state in the characteristic function representation, and are pushed closer to the origin by compressing the state.

This cannot be mimicked by semiclassical interference, where the underlying state is a mixture of pure Gaussian states distributed along $\mathrm{Re}[\beta]$ in the Wigner function. Moreover, by implementing one-dimensional Fourier transformation along $\mathrm{Im}[\nu] = 0$, we can directly obtain the marginal distribution of Wigner function along $\mathrm{Im}[\beta]$ corresponding to momentum statistics and witness high-frequency components corresponding to sub-Planck structure in phase space, which is an intrinsically quantum non-Gaussian attribute caused by the interference [2]. In addition, we extract parity $\langle\hat{\mathcal{P}}\rangle = -0.6 \pm 0.02$ for the odd cat states, by integrating over the full characteristic function. Therefore, it is evident that nonzero values in these interference blobs in the characteristic function representation necessarily correspond to quantum non-Gaussian interference.

We herein use direct measurements of the interference blob amplitude in the characteristic function to quantify the quantum non-Gaussianity of our states. To investigate the effects of phase-space compression against photon loss, we monitor the decay of the blob amplitude for an odd cat state with different degrees of compression over a duration comparable to the cavity single-photon lifetime. For each point in time, we measure a 1D cut of the real part of the characteristic functions to extract the amplitude of the interference blobs. The results are shown in Fig. 4(a), along with simulated theoretical curves, for the uncompressed cat state and three compressed cat states. Our experimental results follow the simulated behavior closely. We observe that they show an exponential reduction in the blob amplitude from its maximum value to the noise floor of the measurement, at a rate that depends on the degree of compression. A theoretical model that captures these dynamics is detailed in Appendix F.

In addition, three snapshots of the characteristic functions are shown in Fig. 4(b) for the cat and compressed cat states, respectively. It is particularly striking that while the interference blobs of the conventional cat states vanish completely at 100 μs, they remain rather prominent in the compressed state with approximately −6.7 dB compression. Furthermore, the compressed cat states preserve their phase-space distribution without any notable distortions throughout their evolution, which is a key requirement for utilizing cat states for information encoding and highlights a crucial advantage of the low anharmonicity regime in which we operate.

Overall, the decay of the quantum non-Gaussian interference is slowed down appreciably for the states with −3, −6.7, and −7.6 dB compression, respectively. Our results closely follow the theoretical predictions based on single-photon loss, at a timescale of 260 μs, being the dominant decoherence channel in the system. Furthermore, we also extract the parity of each state over time by integrating over the full characteristic function, which shows excellent agreement with the timescales obtained by the direct measurements from characteristic functions; see Appendix G.

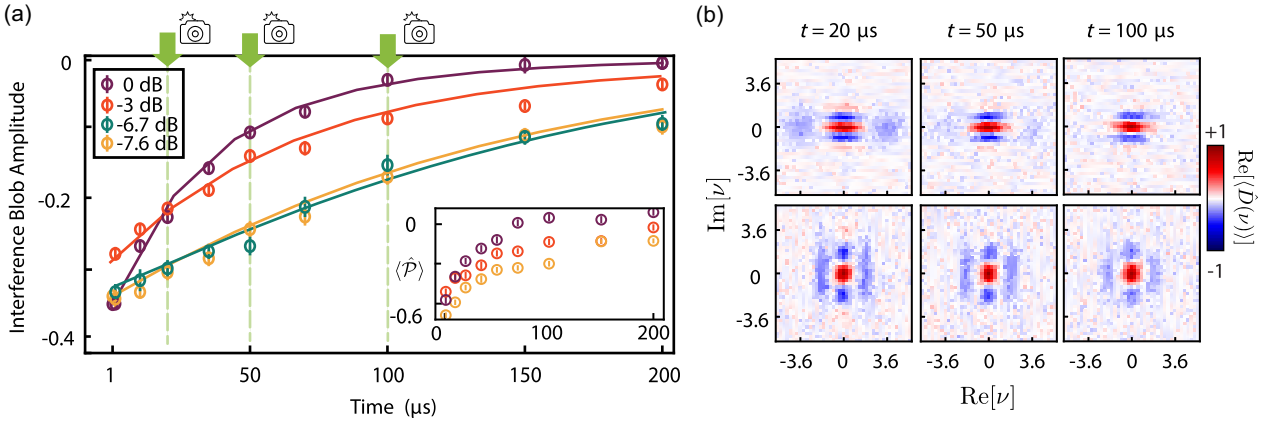

FIG. 4. Time dynamics of interference features in the presence of intrinsic losses in the hardware. (a) The measured contrast (marker) of the blobs in the characteristic functions of odd cat states with 0, −3, −6.7, and −7.6 dB of compression along Re[ν]. The decay is significantly slower for the compressed cat states, which demonstrates that compression and the resulting compactness in phase space protects the quantum interference features in cat states. The measured contrast agrees closely with the master equation simulation (solid lines) with cavity photon loss as the dominant error. Analytical expression provided in Appendix F models the short-time dynamics of our data accurately. Inset: the equivalent decay of the photon number parity $\langle\hat{\mathcal{P}}\rangle$ extracted from the Wigner functions of the same set of states; see Appendix E. The preservation of the odd parity indicates that compressed cat states are more resilient toward photon loss, in agreement with the metric obtained using characteristic functions. All associated uncertainties are extracted by standard bootstrapping techniques. (b) Selected characteristic functions at different decay times, showing the effective preservation of the blobs due to compression.

In summary, we showcase a versatile technique to perform phase-space compression, using repeated applications of ECD gates together with single qubit rotations, both of which are readily accessible in standard cQED hardware. We create various compressed cat states based on this technique and sculpt their quantum non-Gaussian features in phase space to be more optimal for the dominant loss mechanism in the system, which is photon loss. We then probe their intrinsically quantum mechanical features by directly measuring specific regions in their characteristic function. We demonstrate that a more compact landscape in phase space significantly enhances the protection of the compressed cat state's quantum non-Gaussian interference features against photon loss.

Our study brings forth valuable insights into both intrinsic dynamics of CV quantum non-Gaussian resource states and useful applications built upon them. Fundamentally, our results demonstrate that the general strategy of reshaping the phase space of quantum states, using optimized ECD operations [62], effectively preserves their quantum features and enhances their resilience against losses in the hardware. The specific technique to create compressed cat states provides a valuable tool for storing and protecting useful non-Gaussian resource states in highly linear bosonic modes in cQED and affords a flexible test bed for exploring fundamental physics [38] and CV-based quantum metrology [7–11]. Specifically, as these compressed cat states have well-defined parity, they are natural candidates for efficient quantum error correction in bosonic modes, where parity is often used as the main error syndrome. They are inherently more robust code words compared to conventional cat states, thanks to their compact phase-space distribution and the resulting protection of their quantum non-Gaussian features against photon loss. This is further investigated in two recent theory proposals [70,71] indicating that squeezed cat states, together with manifold stabilization, offer a promising path toward protected logical qubits encoded in superconducting cavities. Our work marks a significant step toward experimentally realizing these new paradigms for quantum error correction and fault-tolerant quantum computing.

We thank Yifan Li, Steven Touzard, and Berge Englert for fruitful discussions related to this work. The quantum amplifier used in this experiment is graciously provided by Dr. Ioan Pop and Dr. Patrick Winkel from Karlsruhe Institute of Technology. This research is supported by the National Research Foundation, Singapore, and the Ministry of Education, Singapore, under the Research Centres of Excellence Programme. F. H. acknowledges funding from JST (Moonshot R&D) (Grant No. JPMJMS2064). R. F. acknowledges funding from Project No. 21-13265X of Czech Science Foundation and the European Union's 2020 research and innovation programme (CSA Coordination and support action, H2020-WIDESPREAD-2020-5) under Grant Agreement No. 951737 (NONGAUSS). Y. Y. G. acknowledges the support of the National Research Foundation Fellowship (NRFF12-2020-0063) and the Ministry of Education (Grant No. 21-0054-P0001), Singapore.

APPENDIX A: DEVICE PARAMETERS

Our device consists of a three-dimensional superconducting microwave cavity, an ancillary transmon, and a planar readout resonator, as shown in Fig. 5. The cavity is machined out of high-purity (4N) aluminum and is a $\lambda/4$ transmission line resonator formed by a center stub and cylindrical walls. The readout resonator is deposited together with the transmon on sapphire using double-angle evaporation. The diced sapphire chip is inserted into the tunnel, with the pads of the transmon slightly extending into the coaxial cavities to provide capacitive coupling. Here, we design a weak dispersive coupling to ensure minimal nonlinearity in the cavity mode, such that it serves as a highly harmonic quantum memory that can store multiphoton states with negligible distortion. The ancillary transmon enables fast control of the single cavity. The low-Q readout resonator, together with a quantum-limited amplifier, allows for fast single-shot measurement.

With the weak dispersive coupling between the transmon and the cavity, we are no longer able to extract χ by standard number-splitting measurements. Instead, we derive it by measuring the rotation of a coherent state in characteristic function space over time. Experimentally, we generate a large coherent state with the transmon in the excited state and allow it to evolve over a variable amount of time. This causes the coherent state to rotate at a rate governed by the dispersive coupling term $\chi\hat{a}^\dagger\hat{a}/2$. We extract the resulting rotation angles by fitting the 2D characteristic function of the coherent state at different evolution times Δt to obtain χ from $\Delta\theta = \chi\Delta t$. The Hamiltonian parameters of the system are summarized in Table I.

The cavity energy relaxation time T_1^c is obtained by measuring the decay of a coherent state over time, as discussed in Ref. [76]. We generate a large coherent state and this state decays with a characteristic rate κ, which is probed by applying a highly selective transmon π pulse conditioned on $|0\rangle$ of cavity to measure the population of the vacuum P_0.

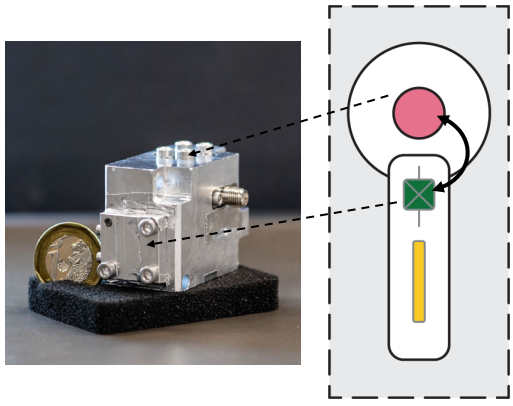

FIG. 5. cQED hardware. Photograph of a device machined out of high-purity aluminum consisting of one storage cavity (pink), single junction transmon (green), and planar readout resonator (gold).

TABLE I. Hamiltonian parameters. Summary of the key system parameters. The nonlinearity of the cavity is below our measurement sensitivity and is extracted from a simulation of the system. RO, readout; Cav, cavity.

	Frequency (GHz)	χ to Transmon	χ to Cav	χ to RO
Transmon	5.1461	205.4 MHz	40 kHz	1 MHz
Cav	6.5428	40 kHz	∼10 Hz	···
RO	7.4418	∼1 MHz	···	···

TABLE II. Coherence parameters. Summary of the coherence timescale of our system's ancillary transmon and storage cavity. State-of-the-art high-Q cavities can commonly achieve T_1^c and T_2^c values of a few ms [76–78].

	T_1 (μs)	T_ϕ (μs)	T_2 (μs)	T_{2e} (μs)
Transmon	20	···	18	20
Cavity	260	≥5000	···	···

For obtaining the cavity T_ϕ^c, we displace the cavity and measure its characteristic function under different decay times as discussed in the Supplemental Material of Ref. [74]. By comparing the measured results with simulations with different T_ϕ^c values, we obtain a bound on T_ϕ^c to be ≥5 ms. This is limited by the residual thermal population of the transmon at ∼1.5%. The coherence parameters of the system are summarized in Table II.

APPENDIX B: COMMUTING COMPRESSION AND CAT STATE CREATION

Here, we illustrate the flexibility of the phase-space manipulation technique demonstrated in this work. While we choose to create a superposition of two compressed coherent states as shown in Fig. 6, we can also first create a cat state and then apply the compression operation subsequently.

The protocol largely remains the same. We initialize the cavity in a cat state and numerically optimize the parameters such that the overlap is maximal with the desired compressed cat state. We simulate this process to verify its practical viability. Using three $\hat{U}\hat{V}$ steps of the $\hat{U}\hat{V}$ operations, we can (in simulation) achieve −3, −5, −6, and −7 dB compression with $\mathcal{F} > 0.99$.

The specific choice of our implementation is made based on practical optimizations for the device's coherence parameters. As a compressed vacuum spans a smaller range of energy levels, our chosen protocol reduces additional cavity decoherence during state creation process. This can be readily modified or adapted to more optimal implementations on cQED hardware with different system parameters.

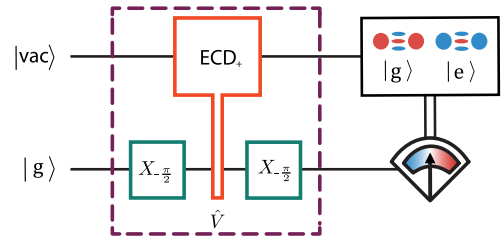

FIG. 6. Cat creation protocol. To create cat states, we use a $\hat{V}$ gate followed by a single-shot qubit readout. Acting with $\hat{V}$ on $|g\rangle|0\rangle$ leaves qubit and cavity in an entangled state where the ground state is entangled to an even cat while the excited state is entangled to an odd cat. Collapsing the qubit with a measurement leaves the cavity in a cat state. To create compressed cat states, we first initialize the cavity into a compressed vacuum state.

APPENDIX C: CHARACTERISTIC FUNCTION MEASUREMENTS

The characteristic function is defined as $C(\nu) = \langle D(\nu)\rangle$. It can be measured directly using conditional displacement operations and single transmon rotations, as discussed in Ref. [74]. The conditional displacement gate is first calibrated by measuring the characteristic function of vacuum state to get a unit displacement amplitude. Experimentally, we do so by adjusting the scaling of the conditional displacements by sweeping amplitude of the displacement gates so that the measured characteristic function of the vacuum state is a Gaussian with standard deviation of $\sigma = 1$. To calibrate the unconditional displacement gate, we can use the forward-and-back sequences [67] consisting of $D(-i\alpha)CD(-1)D(i\alpha)CD(1)$ with the cavity initially in the vacuum state and transmon in $|g\rangle + |e\rangle$. This procedure displaces the cavity to a coherent state first and then back to the vacuum state in the end such that a geometrical phase is accumulated. We measure the expectation value of σ_x by varying α to find the appropriate amplitude scaling for an unconditional displacement $\alpha = 1$, which corresponds to an oscillation with period of $1/\pi$.

APPENDIX D: COMPRESSED VACUUM CREATION

The compressed vacuum states are generated via a deterministic protocol, as proposed in Ref. [72]. It consists of multiple repetitions of the two unitary gates $\hat{U}_k = \exp(iu_k\hat{P}\hat{\sigma}_x)$ and $\hat{V}_k = \exp(iv_k\hat{X}\hat{\sigma}_y)$, with $\hat{X} = (\hat{a} + \hat{a}^\dagger)/2$ and $\hat{P} = i(\hat{a}^\dagger - \hat{a})/2$. The unitaries $\hat{U}_k$ and $\hat{V}_k$ are essentially conditional displacements in opposite directions in phase space, sandwiched by transmon rotations.

The key to generate compressed vacuum states is to choose the ideal number of repetitions along with numerically optimized interaction coefficients u_k and v_k. While more repetitions translate into higher achievable compression in theory, the increased gate time has to be balanced against the dominant decoherence timescale. In our case, the transmon decoherence T_{2e}^q is the main limiting factor. For the results presented in this paper, we choose three repetitions, with each $\hat{U}\hat{V}$ step taking ∼1.37 μs.

In the proposed protocol, the more repetitions of the $\hat{U}\hat{V}$ operations are applied, the closer the resulting state would be to a genuinely squeezed vacuum. However, in the limit of only three repetitions, the final states are only approximately squeezed, with some outlying non-Gaussian features in the phase space. However, these states are effectively compressed in the desired quadrature, with a reduction in their distribution consistent with up to −7.6 dB of compression. Therefore, the presence of nonperfect squeezing is not a hindrance to our scheme, as the protection of the quantum interference features arises from the state being more compact in phase space and is not dependent on the degree of genuine squeezing.

To generate the coefficients u_k, v_k, we numerically optimize them such that the final state has maximal overlap with a target squeezed state, with additional cost parameters given by the physical constraints in our system, such as the maximally achievable ECD displacement for a given gate time. In simulation, the states generated by the protocol have overlaps of $\mathcal{F} > 0.99$ with respect to the target state. The optimized parameters for target squeezed states with −3, −5, −6, and −7 dB can be found in Table III.

The corresponding quadrature compression values in decibels are given in Table IV. They indicate that three repetitions of $\hat{U}\hat{V}$ allow the creation of compressed vacuum states with compression close to the corresponding ideal squeezed state. The experimental compression values are extracted by Gaussian fits to 1D cuts along each quadrature. We then calculate the level of compression by $20\log_{10}[\sigma/\sigma_{\mathrm{vac}}]$.

It is important to note that the optimization process does not take into account the noise model of the hardware.

TABLE III. Summary of optimized coefficients.

	u_1	v_1	u_2	v_2	u_3	v_3
−3 dB	1.39	−0.51	−0.2	0.46	−0.32	0.65
−5 dB	−0.48	−0.51	−1.85	0.31	0.56	−0.91
−6 dB	1.6	−0.39	−0.48	1.04	−1.11	−0.32
−7 dB	−0.83	−0.56	1.3	0.56	−1.26	−0.39

TABLE IV. Summary of achieved compression on vacuum state.

	Theory		Experiment	
	$\langle\hat{P}^2\rangle$	$\langle\hat{X}^2\rangle$	Compression in $\hat{P}$	Compression in $\hat{X}$
−3 dB	2.96	−2.98	2.6	−3
−6 dB	5.71	−5.93	5.4	−6.7
−7 dB	5.9	−7.24	6.4	−7.6

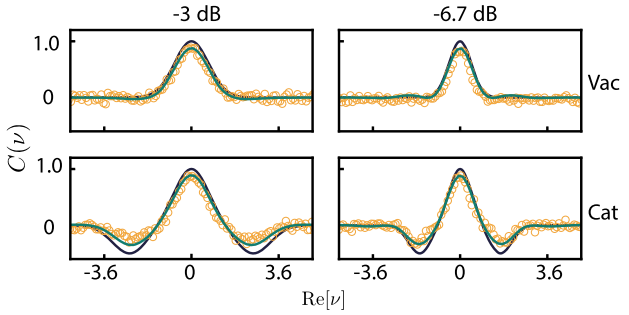

FIG. 7. Comparison of simulated and measured characteristic functions. Black lines (green lines) indicate simulated characteristic function of compressed states without loss (with transmon T_{2e}^{q}). Gold circles denote experimental data. The simulation with loss is scaled with the data contrast. The appearance of side loops is clearly visible and consistent between data and simulated behavior.

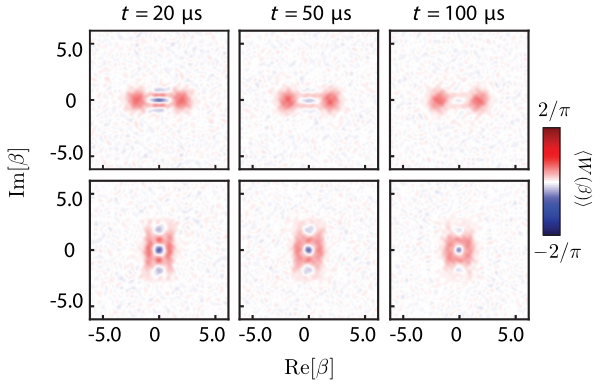

FIG. 8. Discrete Fourier transformation. Wigner function of odd cat with 0 dB (top) and −7.6 dB (bottom) compression at the decay time of 20, 50, and 100 μs, respectively.

Therefore, due to the decoherence of the transmon, we observe a slight deviation from the target state. To verify this, we show the real part of 1D characteristic function cuts of the compressed vacuum states (−3 and −6.7 dB) in Fig. 7. The appearance of side loops can be clearly seen in the simulation and data of the −6.7 dB state. These reduce the amount of real squeezing along the cut. The simulation curves are scaled using the origin point of the measured characteristic functions.

APPENDIX E: COMPARISON OF DIFFERENT METRICS FOR NONCLASSICALITY

Here, we compare the methods of extracting the quantum interference features of the cat and compressed cat states of amplitude $\alpha = 1.8$. More specifically, we analyze the corresponding Wigner functions, sub-Planck structures, and fidelities from reconstructed density matrices and direct integration of the characteristic function over the phase space.

1. Wigner function reconstruction

We obtain the Wigner function $W(\beta)$ from the characteristic function $C(\nu)$ by performing two-dimensional discrete Fourier transform of $C(\nu)$ based on the following equation:

$$W(\beta) = \frac{1}{\pi^2}\int C(\nu)e^{\beta\nu^* - \beta^*\nu}d^2\nu. \tag{E1}$$

Prior to the discrete Fourier transform, we pad the raw characteristic function data with zeros outside the measurement range. This allows a more accurate transformation between the two representations by extending phase space beyond the measurement range. The resulting Wigner functions for an odd cat state and a −7.6 dB. compressed odd cat state at three different decay times are shown in Fig. 8. These Wigner functions closely resemble the expected behaviors as shown in the main text, illustrated by the direct characteristic measurements. We observe that the quantum interference features, denoted here by the presence of Wigner negativity, are substantially more pronounced in the compressed cat state after 100 μs decay time compared to that of the cat state.

Furthermore, we can directly obtain the photon number parity of odd cat states from the value of the Wigner functions at the origin of phase space $W(0,0)$ by fully integrating over the characteristic function, according to Eq. (E1). Their time dynamics [Fig. 4(a), inset] closely echoes that of the decay of interference blob amplitudes extracted directly from the characteristic functions. We observe that with phase-space compression, the parity decays significantly more slowly in the presence of photon loss while the parity of the conventional cat state diminishes to zero rapidly.

2. Sub-Planck phase-space structure

Another useful tool to witness nonclassical interference is the presence of high-frequency components corresponding to sub-Planck structures in phase space [2]. In order to extract this feature from the measured characteristic functions, we implement one-dimensional Fourier transformation along $\mathrm{Im}[\nu] = 0$ and compare it to the same features extracted from the vacuum state.

Here, we illustrate the behavior of the cat and a −7.6 dB compressed cat state at times 1, 20, 50, and 100 μs. For the compressed cat [Fig. 9(b)], the nonclassical sub-Planck structures are still notably present at 100 μs. However, for the cat states [Fig. 9(a)], the sub-Planck features vanish rapidly and are no longer visible at 100 μs. From these results, we again confirm that the quantum non-Gaussian features of compressed cat states are significantly better preserved compared to uncompressed cat states.

3. Density matrix reconstruction

We reconstruct the density matrices of the states using convex optimization [79] with the measured characteristic

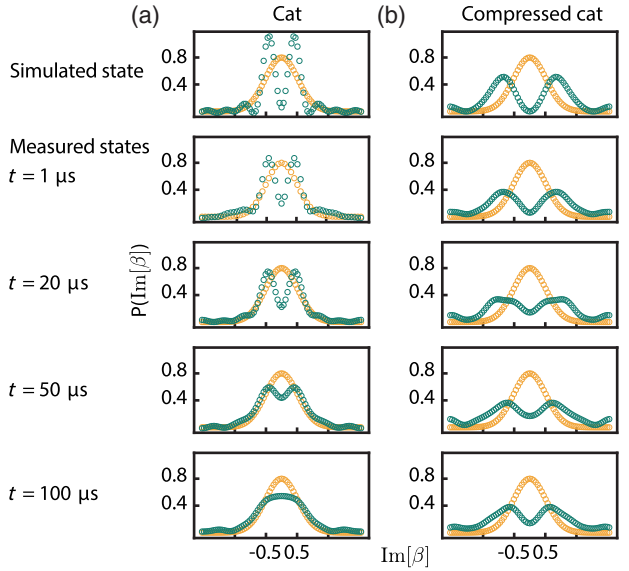

FIG. 9. Decay of sub-Planck structure. We implement a one-dimensional Fourier transformation along $\mathrm{Im}[\nu] = 0$ of the ideal (top row) and measured characteristic function. We obtain the marginal momentum distribution of $\mathrm{Im}[\beta]$ for (a) cat (green) and (b) −7.6 dB compressed cat (green) of different decay times, respectively, and compare the width of resulting oscillatory features to that of ideal vacuum (gold).

functions as the input. We experimentally verify that the imaginary components of the characteristic functions are negligible (i.e., within measurement noise) and perform reconstruction using the real parts for an odd cat state and a compressed cat state at decay times 1, 20, 50, and 100 μs with 1000 averages per point each. The Hilbert space size 20 chosen for the reconstruction protocol is based on simulations of photon number distributions of ideal cat states with the same amplitude. The fidelities $\mathcal{F}_{\mathrm{cat,rec}}$ ($\mathcal{F}_{\mathrm{ccat,rec}}$), defined as the overlap of the ideal cat (compressed cat) state and the experimentally reconstructed density matrices, are shown in Table V. The associated uncertainties in these values are computed using standard bootstrapping techniques.

Once more, we observe that $\mathcal{F}_{\mathrm{cat,rec}}$ decays more rapidly compared to $\mathcal{F}_{\mathrm{ccat,rec}}$. For instance, as the decay time increases from 1 to 20 μs, the fidelity of cat state decreases sharply from 75% to 55%. In contrast, for the compressed cat state, the fidelity drops notably more slowly from 61% to 56%.

TABLE V. Comparison of fidelities extracted from density matrix reconstruction ($\mathcal{F}_{\mathrm{cat,rec}}$) and direct integration of characteristic function ($\mathcal{F}_{\mathrm{cat,int}}$).

State	$\mathcal{F}_{\mathrm{cat,rec}}$ (%)	$\mathcal{F}_{\mathrm{cat,int}}$ (%)	$\mathcal{F}_{\mathrm{ccat,rec}}$ (%)	$\mathcal{F}_{\mathrm{ccat,int}}$ (%)
1 μs	75 (±0.5)	74.8 (±0.6)	61 (±0.7)	67.1 (±0.7)
20 μs	55 (±0.6)	61.52 (±0.8)	56 (±0.5)	60.4 (±0.7)
50 μs	45 (±0.7)	47.88 (±0.7)	50 (±0.6)	53.9 (±0.6)
100 μs	40 (±0.7)	41.15 (±0.7)	43 (±0.5)	46.4 (±0.7)

4. Direct integration over phase space

An alternative method to calculate the fidelity of states of interest is by directly integrating the characteristic function over the phase space. For a state with characteristic function $C_{\mathrm{exp}}(\nu)$, we compute this overlap to the ideal target state $C_{\mathrm{ideal}}(\nu)$ using the following equation:

$$\mathcal{F}_{\mathrm{int}} = \frac{1}{\pi}\int C_{\mathrm{ideal}}(\nu)C_{\mathrm{exp}}(\nu)^* d^2\nu. \tag{E2}$$

The calculated fidelities of cats $\mathcal{F}_{\mathrm{cat,int}}$ and compressed cats $\mathcal{F}_{\mathrm{ccat,int}}$ at different decay times are presented in Table. V. These are consistent with the fidelities obtained from density matrix reconstruction, in which the compressed cat state retains its fidelity much better in the presence of photon loss.

APPENDIX F: DYNAMIC OF INTERFERENCE FEATURE

To derive the scaling of the maxima of the interference blob amplitudes in the characteristic function corresponding to the momentum interference fringe in the Wigner function [80] for compressed and attenuated even or odd cat state, we start from the marginal characteristic function,

$$\begin{aligned} C_{\pm,s,\tau}(0,\nu_p) = {} & e^{-(1-\eta)\nu_p^2/2}/(2 \pm 2e^{|\alpha_0|^2}) \\ & \times (2e^{-\eta\nu_p^2/2s^2} \pm e^{-(s|\alpha_0|-\sqrt{\eta}\nu_p)^2/2s^2} \\ & \pm e^{-(s|\alpha_0|+\sqrt{\eta}\nu_p)^2/2s^2}), \end{aligned} \tag{F1}$$

where ± stands for even or odd parity of the cat, $\nu_p = \mathrm{Im}[\nu]/\sigma_0$ is the normalized frequency of oscillations in the momentum marginal distribution, $\alpha_0 = \alpha/\sigma_0$ is the normalized amplitude of coherent state, $s = \exp[-\tau_s/(2T_1^c)]$ is (linear) amplitude compression factor, τ_s is (exponential) compression factor, $\eta = \exp(-\tau/T_1^c)$ is amplitude damping factor η as function of time τ, and σ_0 is a standard deviation of the ground state extension in the position or momentum quadrature of the field. We can find a ratio that connects with the initial undamped cat at $\tau = 0$ with the same compression factor s,

$$F_{\pm,s,\tau} = \frac{C_{\pm,s,\tau}(0,\nu_p)}{C_{\pm,s,0}(0,\nu_p)} = \exp\left(-\frac{1}{2}(e^{\tau/T_1^c}-1)s^2|\alpha_0|^2\right), \tag{F2}$$

for both the even and odd cats. Evidently, smaller s makes the fidelity $F_{\pm,s,\tau}$ to *asymptotically* approach unity and brings the blobs to their maximal amplitudes as both τ and α_0 increase. Moreover, smaller s corresponding to larger

compression is required for larger α_0 and larger τ to reach fidelity $F_{\pm,s,\tau} \to 1$.

For a short time $\tau \ll T_1^c$, we already witness the scaling,

$$F_{\pm,s,\tau} \approx \exp\left(-\frac{\tau}{2T_{\text{eff}}}|\alpha_0|^2\right), \tag{F3}$$

where $T_{\text{eff}} = T_1^c/s^2$ is the effective decay constant corresponding to each of the compressed cat states. Using this model, we observe that T_{eff} for the uncompressed cat is 273 ± 13 μs, consistent with the intrinsic photon lifetime of the cavity. In contrast, the T_{eff} is significantly enhanced to 516 ± 32, 1247 ± 132, and 1439 ± 172 μs for the -3, -6.7, and -7.6 dB compressed cat states, respectively.

On the other hand, for long time $\tau \gg T_1^c$,

$$F_{\pm,s,\tau} \approx \exp\left(-\frac{1}{2}e^{(\tau-\tau_s)/T_1^c}|\alpha_0|^2\right), \tag{F4}$$

the (exponential) compression factor τ_s effectively reduces the time τ of decay. These characteristics fully describe maxima of the interference blobs in the characteristic function.

However, lower s naturally extends the overall $C_{\pm,s,\tau}(\nu_x, \nu_p)$ in the frequencies ν_x of the position marginal distribution. Subsequently, such higher ν_x is filtered out by the cavity decay acting symmetrically on both the ν_x and ν_p frequencies. It complementarily reduces the amplitudes of the coherent states in the superposition, as their interference effect is preserved. To universally compromise it for larger α_0, the compression can approximately symmetrize the contours of both Wigner and characteristic functions when $s = |\alpha_0|^{-1}$. In this case, we obtain a compromise scaling for the fidelity of interference blobs,

$$F_{\pm,s=|\alpha|^{-1},\tau} \approx \exp\left[-\frac{1}{2}(e^{\tau/T_1^c} - 1)\right], \tag{F5}$$

in a universal form, irrespective to an arbitrarily large $|\alpha_0|$. The interference bulbs then do not decay faster for larger $|\alpha_0|$. Therefore, any cat state will decay in the interference bulbs with the help of the compression as a small kitten with $\alpha_0 = 1$ does.

Similarly, we can translate the analysis for parity decay depending on cat size and compression. This recovers the expression derived in Ref. [61].

APPENDIX G: IDEAL COMPRESSION FOR PARITY PROTECTION

Photon loss acts as a low-pass filter with a 2D Gaussian profile in phase space. For the preservation of interference features of cat states, the more strongly compressed (i.e., closer to the origin in phase space), the more pronounced the protection is. However, for the photon number parity, which is an important observable used in quantum error correction schemes, the resulting elongation in the opposite quadrature due to strong compression in phase space causes the cat states to exceed the range of the Gaussian filter.

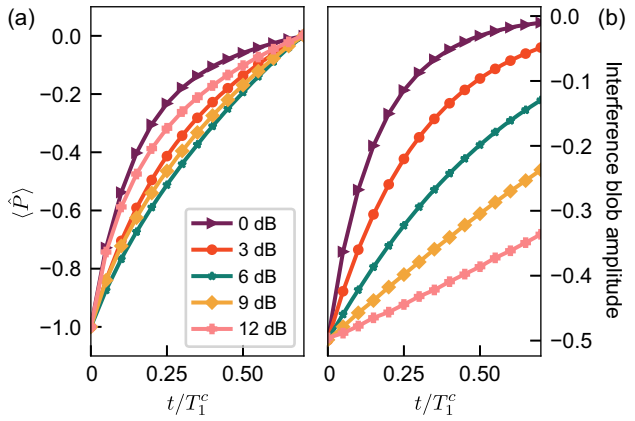

FIG. 10. Simulation result of decay of photon number parity and interference blob amplitude. Parity decay (a) and interference blob decay in the characteristic function (b) for cat states with different degrees of compression. While there exists an optimal compression level to protect parity, the decay of interference blob is consistently slower as compression increases.

Here, we investigate this effect by simulating the behavior of the interference blobs and the photon number parity of a cat state under different compression levels as shown in Fig. 10. In the case of the interference blob amplitude, the decay becomes consistently slower as we increase the compression in phase space. In comparison, the reduction in parity is mitigated by the compression up to -6 dB. Further compression leads to an acceleration in its parity decay, due to the extension in the opposite direction in phase space beyond the Gaussian filter. As the photon number parity requires integration over the entire characteristic function, it is sensitive to the elongation of the state under compression. Therefore, for the preservation of parity, there exists an optimal compression level that is determined by the photon loss rate in the system and the size of the cat state.

APPENDIX H: ERROR BUDGET

The fidelities of the compressed cat states we create in this work, extracted using the different methods mentioned in Appendix E, are generally in the range of $65(\pm 5)\%$. This is largely limited by the decoherence timescales in our hardware. To analyze this, we choose the action of a single $\hat{U}$ gate as the base for gauging the imperfections involved in our state creation and measurement process, which are essentially $\hat{U}$ or $\hat{V}$ operations sandwiched between single transmon rotations. The fidelities are calculated as the overlap of the ideal state with the overlap of the state suffering from a single decoherence mechanism $\mathcal{F} = \langle \psi_{\text{ideal}}|\rho_{\text{loss}}|\psi_{\text{ideal}}\rangle$. The simulated infidelities due to the different sources of nonidealities in the device are shown in Table VI. They are calculated via master equation simulations which include only the respective decoherence mechanism.

TABLE VI. Error budget. Estimated infidelities due to SPAM (state preparation and measurement) errors of our cats and compressed cat states. Ancilla dephasing and decay together with readout errors are the dominant sources of error in our system.

Error channel	Estimated infidelity (%)
Ancilla dephasing	4
Ancilla decay	2
Cavity dephasing	1
Cavity decay	0.01
$\hat{U}$	≈7
Readout $\|g\rangle \rightarrow \|g\rangle$	1.4
Readout $\|e\rangle \rightarrow \|e\rangle$	5

First, let us compare this proposed error budget with experimentally observed imperfections in our characteristic function measurement. In our results, the measured vacuum state shows a maximum contrast of ≈88.4%. The implementation requires a single $\hat{U}$-type gate and a transmon readout. Summing up the individual contributions, we expect the $\hat{U}$ operation to have an infidelity ≈7% and a readout infidelity of $(P_{ee} + P_{gg})/2 \approx 3.2\%$. This results in an overall limit on the measurement fidelity to ≈90%, which is consistent with the contrast of the measured vacuum state. We use this as a normalization factor for the subsequent data of the cat and compressed cat state creation to isolate the state preparation errors from that of the measurement.

For the compressed vacuum and cat states shown in the main text, the state creation process involves three sets of $\hat{U}\,\hat{V}$ operations and one measurement to project the transmon state. The postselection process after this measurement effectively removes the contribution of transmon T_1^q, making the fidelity of each $\hat{U}$ or $\hat{V}$ gate approximately 5%. Therefore, using the simulated error budgets, we expect them to suffer from ≈33% infidelity, which is again consistent with the data we present.

While decoherence is the dominant limitation, other mechanisms such as the Kerr effect, calibration inaccuracies, and residual imaginary components in the characteristic functions, etc. could also introduce some imperfections to states we consider here. However, as these are small compared to decoherence errors, we do not have the resolution to analyze them in detail. Overall, if this protocol is applied on a system with better coherence parameters, then investigating and minimizing these imperfections will become more crucial.

[1] E. Schrödinger, *Die Gegenwärtige Situation in der Quantenmechanik*, Naturwissenschaften **23**, 844 (1935).

[2] W. H. Zurek, *Sub-Planck Structure in Phase Space and Its Relevance for Quantum Decoherence*, Nature (London) **412**, 712 (2001).

[3] W. Schleich, M. Pernigo, and F. L. Kien, *Nonclassical State from Two Pseudoclassical States*, Phys. Rev. A **44**, 2172 (1991).

[4] C. Gerry and P. Knight, *Quantum Superpositions and Schrödinger Cat States in Quantum Optics*, Am. J. Phys. **65**, 964 (1997).

[5] W. Qin, A. Miranowicz, H. Jing, and F. Nori, *Generating Long-Lived Macroscopically Distinct Superposition States in Atomic Ensembles*, Phys. Rev. Lett. **127**, 093602 (2021).

[6] J.-M. Raimond and S. Haroche, *Exploring the Quantum* (Oxford University Press, 2006), Vol. 82, p. 86.

[7] W. J. Munro, K. Nemoto, G. J. Milburn, and S. L. Braunstein, *Weak-Force Detection with Superposed Coherent States*, Phys. Rev. A **66**, 023819 (2002).

[8] J. Joo, W. J. Munro, and T. P. Spiller, *Quantum Metrology with Entangled Coherent States*, Phys. Rev. Lett. **107**, 083601 (2011).

[9] A. Facon, E.-K. Dietsche, D. Grosso, S. Haroche, J.-M. Raimond, M. Brune, and S. Gleyzes, *A Sensitive Electrometer Based on a Rydberg Atom in a Schrödinger-Cat State*, Nature (London) **535**, 262 (2016).

[10] P. A. Knott, T. J. Proctor, A. J. Hayes, J. P. Cooling, and J. A. Dunningham, *Practical Quantum Metrology with Large Precision Gains in the Low-Photon-Number Regime*, Phys. Rev. A **93**, 033859 (2016).

[11] K. Duivenvoorden, B. M. Terhal, and D. Weigand, *Single-Mode Displacement Sensor*, Phys. Rev. A **95**, 012305 (2017).

[12] S. J. van Enk and O. Hirota, *Entangled Coherent States: Teleportation and Decoherence*, Phys. Rev. A **64**, 022313 (2001).

[13] H. Jeong, M. S. Kim, and J. Lee, *Quantum-Information Processing for a Coherent Superposition State via a Mixed Entangled Coherent Channel*, Phys. Rev. A **64**, 052308 (2001).

[14] N. Sangouard, C. Simon, N. Gisin, J. Laurat, R. Tualle-Brouri, and P. Grangier, *Quantum Repeaters with Entangled Coherent States*, J. Opt. Soc. Am. B **27**, A137 (2010).

[15] J. B. Brask, I. Rigas, E. S. Polzik, U. L. Andersen, and A. S. Sørensen, *Hybrid Long-Distance Entanglement Distribution Protocol*, Phys. Rev. Lett. **105**, 160501 (2010).

[16] S.-W. Lee and H. Jeong, *Near-Deterministic Quantum Teleportation and Resource-Efficient Quantum Computation Using Linear Optics and Hybrid Qubits*, Phys. Rev. A **87**, 022326 (2013).

[17] T. C. Ralph, A. Gilchrist, G. J. Milburn, W. J. Munro, and S. Glancy, *Quantum Computation with Optical Coherent States*, Phys. Rev. A **68**, 042319 (2003).

[18] A. P. Lund, T. C. Ralph, and H. L. Haselgrove, *Fault-Tolerant Linear Optical Quantum Computing with Small-Amplitude Coherent States*, Phys. Rev. Lett. **100**, 030503 (2008).

[19] Z. Leghtas, G. Kirchmair, B. Vlastakis, R. J. Schoelkopf, M. H. Devoret, and M. Mirrahimi, *Hardware-Efficient Autonomous Quantum Memory Protection*, Phys. Rev. Lett. **111**, 120501 (2013).

[20] M. Mirrahimi, Z. Leghtas, V. V. Albert, S. Touzard, R. J. Schoelkopf, L. Jiang, and M. H. Devoret, *Dynamically Protected Cat-Qubits: A New Paradigm for Universal Quantum Computation*, New J. Phys. **16**, 045014 (2014).

[21] Z. Leghtas, S. Touzard, I. M. Pop, A. Kou, B. Vlastakis, A. Petrenko, K. M. Sliwa, A. Narla, S. Shankar, M. J. Hatridge *et al.*, *Confining the State of Light to a Quantum Manifold by Engineered Two-Photon Loss*, Science **347**, 853 (2015).

[22] N. Ofek, A. Petrenko, R. Heeres, P. Reinhold, Z. Leghtas, B. Vlastakis, Y. Liu, L. Frunzio, S. Girvin, L. Jiang *et al.*, *Extending the Lifetime of a Quantum Bit with Error Correction in Superconducting Circuits*, Nature (London) **536**, 441 (2016).

[23] S. Puri, S. Boutin, and A. Blais, *Engineering the Quantum States of Light in a Kerr-Nonlinear Resonator by Two-Photon Driving*, npj Quantum Inf. **3**, 18 (2017).

[24] S. Touzard, A. Grimm, Z. Leghtas, S. O. Mundhada, P. Reinhold, C. Axline, M. Reagor, K. Chou, J. Blumoff, K. M. Sliwa, S. Shankar, L. Frunzio, R. J. Schoelkopf, M. Mirrahimi, and M. H. Devoret, *Coherent Oscillations Inside a Quantum Manifold Stabilized by Dissipation*, Phys. Rev. X **8**, 021005 (2018).

[25] S. Puri, A. Grimm, P. Campagne-Ibarcq, A. Eickbusch, K. Noh, G. Roberts, L. Jiang, M. Mirrahimi, M. H. Devoret, and S. M. Girvin, *Stabilized Cat in a Driven Nonlinear Cavity: A Fault-Tolerant Error Syndrome Detector*, Phys. Rev. X **9**, 041009 (2019).

[26] J. Guillaud and M. Mirrahimi, *Repetition Cat Qubits for Fault-Tolerant Quantum Computation*, Phys. Rev. X **9**, 041053 (2019).

[27] A. Grimm, N. E. Frattini, S. Puri, S. O. Mundhada, S. Touzard, M. Mirrahimi, S. M. Girvin, S. Shankar, and M. H. Devoret, *Stabilization and Operation of a Kerr-Cat Qubit*, Nature (London) **584**, 205 (2020).

[28] S. Puri, L. St-Jean, J. A. Gross, A. Grimm, N. E. Frattini, P. S. Iyer, A. Krishna, S. Touzard, L. Jiang, A. Blais *et al.*, *Bias-Preserving Gates with Stabilized Cat Qubits*, Sci. Adv. **6**, eaay5901 (2020).

[29] R. Lescanne, M. Villiers, T. Peronnin, A. Sarlette, M. Delbecq, B. Huard, T. Kontos, M. Mirrahimi, and Z. Leghtas, *Exponential Suppression of Bit-Flips in a Qubit Encoded in an Oscillator*, Nat. Phys. **16**, 509 (2020).

[30] C. Chamberland, K. Noh, P. Arrangoiz-Arriola, E. T. Campbell, C. T. Hann, J. Iverson, H. Putterman, T. C. Bohdanowicz, S. T. Flammia, A. Keller, G. Refael, J. Preskill, L. Jiang, A. H. Safavi-Naeini, O. Painter, and F. G. S. L. Brandão, *Building a Fault-Tolerant Quantum Computer Using Concatenated Cat Codes*, PRX Quantum **3**, 010329 (2022).

[31] A. Ourjoumtsev, H. Jeong, R. Tualle-Brouri, and P. Grangier, *Generation of Optical 'Schrödinger Cats' from Photon Number States*, Nature (London) **448**, 784 (2007).

[32] A. Ourjoumtsev, F. Ferreyrol, R. Tualle-Brouri, and P. Grangier, *Preparation of Non-Local Superpositions of Quasi-Classical Light States*, Nat. Phys. **5**, 189 (2009).

[33] K. Huang, H. Le Jeannic, J. Ruaudel, V. B. Verma, M. D. Shaw, F. Marsili, S. W. Nam, E. Wu, H. Zeng, Y.-C. Jeong, R. Filip, O. Morin, and J. Laurat, *Optical Synthesis of Large-Amplitude Squeezed Coherent-State Superpositions with Minimal Resources*, Phys. Rev. Lett. **115**, 023602 (2015).

[34] W. Asavanant, K. Nakashima, Y. Shiozawa, J.-I. Yoshikawa, and A. Furusawa, *Generation of Highly Pure Schrödinger's Cat States and Real-Time Quadrature Measurements via Optical Filtering*, Opt. Express **25**, 32227 (2017).

[35] M. Wang, M. Zhang, Z. Qin, Q. Zhang, L. Zeng, X. Su, C. Xie, and K. Peng, *Experimental Preparation and Manipulation of Squeezed Cat States via an All-Optical In-Line Squeezer*, Laser Photonics Rev. **16**, 2200336 (2022).

[36] D. J. Wineland, *Nobel Lecture: Superposition, Entanglement, and Raising Schrödinger's Cat*, Rev. Mod. Phys. **85**, 1103 (2013).

[37] D. Kienzler, C. Flühmann, V. Negnevitsky, H.-Y. Lo, M. Marinelli, D. Nadlinger, and J. P. Home, *Observation of Quantum Interference between Separated Mechanical Oscillator Wave Packets*, Phys. Rev. Lett. **116**, 140402 (2016).

[38] S. Haroche, *Nobel Lecture: Controlling Photons in a Box and Exploring the Quantum to Classical Boundary*, Rev. Mod. Phys. **85**, 1083 (2013).

[39] S. Deleglise, I. Dotsenko, C. Sayrin, J. Bernu, M. Brune, J.-M. Raimond, and S. Haroche, *Reconstruction of Non-Classical Cavity Field States with Snapshots of Their Decoherence*, Nature (London) **455**, 510 (2008).

[40] B. Vlastakis, G. Kirchmair, Z. Leghtas, S. E. Nigg, L. Frunzio, S. M. Girvin, M. Mirrahimi, M. H. Devoret, and R. J. Schoelkopf, *Deterministically Encoding Quantum Information Using 100-Photon Schrödinger Cat States*, Science **342**, 607 (2013).

[41] C. Wang, Y. Y. Gao, P. Reinhold, R. W. Heeres, N. Ofek, K. Chou, C. Axline, M. Reagor, J. Blumoff, K. Sliwa *et al.*, *A Schrödinger Cat Living in Two Boxes*, Science **352**, 1087 (2016).

[42] R. W. Heeres, B. Vlastakis, E. Holland, S. Krastanov, V. V. Albert, L. Frunzio, L. Jiang, and R. J. Schoelkopf, *Cavity State Manipulation Using Photon-Number Selective Phase Gates*, Phys. Rev. Lett. **115**, 137002 (2015).

[43] S. Krastanov, V. V. Albert, C. Shen, C.-L. Zou, R. W. Heeres, B. Vlastakis, R. J. Schoelkopf, and L. Jiang, *Universal Control of an Oscillator with Dispersive Coupling to a Qubit*, Phys. Rev. A **92**, 040303(R) (2015).

[44] P. Krantz, M. Kjaergaard, F. Yan, T. P. Orlando, S. Gustavsson, and W. D. Oliver, *A Quantum Engineer's Guide to Superconducting Qubits*, Appl. Phys. Rev. **6**, 021318 (2019).

[45] M. Kjaergaard, M. E. Schwartz, J. Braumüller, P. Krantz, J. I.-J. Wang, S. Gustavsson, and W. D. Oliver, *Superconducting Qubits: Current State of Play*, Annu. Rev. Condens. Matter Phys. **11**, 369 (2020).

[46] A. Blais, A. L. Grimsmo, S. M. Girvin, and A. Wallraff, *Circuit Quantum Electrodynamics*, Rev. Mod. Phys. **93**, 025005 (2021).

[47] A. J. Leggett, S. Chakravarty, A. T. Dorsey, M. P. Fisher, A. Garg, and W. Zwerger, *Dynamics of the Dissipative Two-State System*, Rev. Mod. Phys. **59**, 1 (1987).

[48] A. O. Caldeira and A. J. Leggett, *Quantum Tunnelling in a Dissipative System*, Ann. Phys. (N.Y.) **149**, 374 (1983).

[49] A. O. Caldeira and A. J. Leggett, *Path Integral Approach to Quantum Brownian Motion*, J. Phys. A **121**, 587 (1983).

[50] A. O. Caldeira and A. J. Leggett, *Influence of Damping on Quantum Interference: An Exactly Soluble Model*, Phys. Rev. A **31**, 1059 (1985).

[51] A. Leggett, *Schrödinger's Cat and Her Laboratory Cousins*, Contemp. Phys. **25**, 583 (1984).

[52] W. H. Zurek, *Pointer Basis of Quantum Apparatus: Into What Mixture Does the Wave Packet Collapse?*, Phys. Rev. D **24**, 1516 (1981).
[53] G. T. Moore and M. O. Scully, *Frontiers of Nonequilibrium Statistical Physics* (Springer Science & Business Media, New York, 2012), Vol. 135.
[54] W. H. Zurek, *From Quantum to Classical*, Phys. Today **44**, No. 10, 36 (1991).
[55] M. S. Kim and V. Bužek, *Schrödinger-Cat States at Finite Temperature: Influence of a Finite-Temperature Heat Bath on Quantum Interferences*, Phys. Rev. A **46**, 4239 (1992).
[56] U. Leonhardt, *Essential Quantum Optics: From Quantum Measurements to Black Holes* (Cambridge University Press, Cambridge, England, 2010).
[57] R. Filip, *Amplification of Schrödinger-Cat State in a Degenerate Optical Parametric Amplifier*, J. Opt. B **3**, S1 (2001).
[58] A. Serafini, S. De Siena, F. Illuminati, and M. G. Paris, *Minimum Decoherence Cat-like States in Gaussian Noisy Channels*, J. Opt. B **6**, S591 (2004).
[59] D. Menzies and R. Filip, *Gaussian-Optimized Preparation of Non-Gaussian Pure States*, Phys. Rev. A **79**, 012313 (2009).
[60] R. Filip, *Gaussian Quantum Adaptation of Non-Gaussian States for a Lossy Channel*, Phys. Rev. A **87**, 042308 (2013).
[61] H. Le Jeannic, A. Cavaillès, K. Huang, R. Filip, and J. Laurat, *Slowing Quantum Decoherence by Squeezing in Phase Space*, Phys. Rev. Lett. **120**, 073603 (2018).
[62] K. Park, J. Hastrup, J. S. Neergaard-Nielsen, J. B. Brask, R. Filip, and U. L. Andersen, *Slowing Quantum Decoherence of Oscillators by Hybrid Processing*, npj Quantum Inf. **8**, 67 (2022).
[63] R. Y. Teh, P. D. Drummond, and M. D. Reid, *Overcoming Decoherence of Schrödinger Cat States Formed in a Cavity Using Squeezed-State Inputs*, Phys. Rev. Res. **2**, 043387 (2020).
[64] J. Etesse, M. Bouillard, B. Kanseri, and R. Tualle-Brouri, *Experimental Generation of Squeezed Cat States with an Operation Allowing Iterative Growth*, Phys. Rev. Lett. **114**, 193602 (2015).
[65] H.-Y. Lo, D. Kienzler, L. de Clercq, M. Marinelli, V. Negnevitsky, B. C. Keitch, and J. P. Home, *Spin–Motion Entanglement and State Diagnosis with Squeezed Oscillator Wavepackets*, Nature (London) **521**, 336 (2015).
[66] C. Flühmann and J. P. Home, *Direct Characteristic-Function Tomography of Quantum States of the Trapped-Ion Motional Oscillator*, Phys. Rev. Lett. **125**, 043602 (2020).
[67] A. Eickbusch, V. Sivak, A. Z. Ding, S. S. Elder, S. R. Jha, J. Venkatraman, B. Royer, S. Girvin, R. J. Schoelkopf, and M. H. Devoret, *Fast Universal Control of an Oscillator with Weak Dispersive Coupling to a Qubit*, Nat. Phys. **18**, 1464 (2022).
[68] A. Joshi, K. Noh, and Y. Y. Gao, *Quantum Information Processing with Bosonic Qubits in Circuit QED*, Quantum Sci. Technol. **6**, 033001 (2021).
[69] D. S. Schlegel, F. Minganti, and V. Savona, *Quantum Error Correction Using Squeezed Schrödinger Cat States*, Phys. Rev. A **106**, 022431 (2022).
[70] Q. Xu, G. Zheng, Y.-X. Wang, P. Zoller, A. A. Clerk, and L. Jiang, *Autonomous Quantum Error Correction and Fault-Tolerant Quantum Computation with Squeezed Cat Qubits*, arXiv:2210.13406.
[71] T. Hillmann and F. Quijandría, *Quantum Error Correction with Dissipatively Stabilized Squeezed Cat Qubits*, arXiv:2210.13359.
[72] J. Hastrup, K. Park, R. Filip, and U. L. Andersen, *Unconditional Preparation of Squeezed Vacuum from Rabi Interactions*, Phys. Rev. Lett. **126**, 153602 (2021).
[73] R. W. Heeres, P. Reinhold, N. Ofek, L. Frunzio, L. Jiang, M. H. Devoret, and R. J. Schoelkopf, *Implementing a Universal Gate Set on a Logical Qubit Encoded in an Oscillator*, Nat. Commun. **8**, 1 (2017).
[74] P. Campagne-Ibarcq, A. Eickbusch, S. Touzard, E. Zalys-Geller, N. E. Frattini, V. V. Sivak, P. Reinhold, S. Puri, S. Shankar, R. J. Schoelkopf *et al.*, *Quantum Error Correction of a Qubit Encoded in Grid States of an Oscillator*, Nature (London) **584**, 368 (2020).
[75] P. Winkel, I. Takmakov, D. Rieger, L. Planat, W. Hasch-Guichard, L. Grünhaupt, N. Maleeva, F. Foroughi, F. Henriques, K. Borisov, J. Ferrero, A. V. Ustinov, W. Wernsdorfer, N. Roch, and I. M. Pop, *Nondegenerate Parametric Amplifiers Based on Dispersion-Engineered Josephson-Junction Arrays*, Phys. Rev. Appl. **13**, 024015 (2020).
[76] M. Reagor, Superconducting Cavities for Circuit Quantum Electrodynamics, Ph.D. thesis, Yale University, 2015.
[77] S. Chakram, K. He, A. V. Dixit, A. E. Oriani, R. K. Naik, N. Leung, H. Kwon, W.-L. Ma, L. Jiang, and D. I. Schuster, *Multimode Photon Blockade*, Nat. Phys. **18**, 879 (2022).
[78] M. Kudra, J. Biznárová, A. Fadavi Roudsari, J. J. Burnett, D. Niepce, S. Gasparinetti, B. Wickman, and P. Delsing, *High Quality Three-Dimensional Aluminum Microwave Cavities*, Appl. Phys. Lett. **117**, 070601 (2020).
[79] I. Strandberg, *Simple, Reliable, and Noise-Resilient Continuous-Variable Quantum State Tomography with Convex Optimization*, Phys. Rev. Appl. **18**, 044041 (2022).
[80] J. Janszky, A. Petak, C. Sibilia, M. Bertolotti, and P. Adam, *Optical Schrodinger-Cat States in a Directional Coupler*, J. Opt. B **7**, 145 (1995).